Journal of ELECTRONIC MATERIALS, Vol. 45, No. 9, 2016
DOI: 10.1007/s11664-016-4545-y
© 2016 The Minerals, Metals & Materials Society

CrossMark

Analysis of III–V Superlattice *n*B*n* Device Characteristics

DAVID R. RHIGER,[1,3] EDWARD P. SMITH,[1] BORYS P. KOLASA,[1]
JIN K. KIM,[2] JOHN F. KLEM,[2] and SAMUEL D. HAWKINS[2]

1.—Raytheon Vision Systems, 75 Coromar Dr., Goleta, CA 93117, USA. 2.—Sandia National Laboratories, P. O. Box 5800, Albuquerque, NM 87185, USA. 3.—e-mail: drhiger@raytheon.com

Mid-wavelength infrared *n*B*n* detectors built with III–V superlattice materials have been tested by means of both capacitance and direct-current methods. By combining the results, it is possible to achieve clear separation of the two components of dark current, namely the generation–recombination (GR) current due to the Shockley–Read–Hall mechanism in the depletion region, and the diffusion current from the neutral region. The GR current component is unambiguously identified by two characteristics: (a) it is a linear function of the depletion width, and (b) its activation energy is approximately one-half the bandgap. The remaining current is shown to be due to diffusion because of its activation energy equaling the full bandgap. In addition, the activation energy of the total measured dark current in each local region of the temperature–bias parameter space is evaluated. We show the benefits of capacitance analysis applied to the *n*B*n* device and review some of the requirements for correct measurements. The carrier concentration of the unintentionally doped absorber region is found to be 1.2×10^{14} cm^{-3} *n*-type. It is shown that the depletion region resides almost entirely within the absorber. Also, the doping in the *n*B*n* barrier is found to be 4×10^{15} cm^{-3} *p*-type. Minority-carrier lifetimes estimated from the dark current components are on the order of 10 μs.

Key words: Infrared, *n*B*n*, III–V material, superlattice, InAs/InAsSb, capacitance measurements

INTRODUCTION

It is evident from recent work that III–V superlattice materials are now under development for application in infrared (IR) detectors.[1–6] One device configuration that makes good use of these materials is the *n*B*n* structure, which consists of an *n*-type absorber region and an *n*-type contact separated by a wide-bandgap barrier (B). The barrier is designed to be unipolar,[7,8] extending into the conduction band to block the flow of majority carrier electrons in either direction, while presenting no impediment in the valence band to the flow of minority carrier holes from the absorber to the contact. In normal operation, IR photons produce electron–hole pairs in the absorber, and a negative bias voltage applied to the contact causes the holes to flow past the barrier to the contact. A substantial reduction in dark current is realized by the use of the barrier, which restricts the current to holes only. Expected applications of the devices discussed in this paper are for detection in the extended mid-wavelength infrared (MWIR) range of 3 μm to 6 μm.

Materials for *n*B*n* devices in most cases are based upon the 6.1-Å family of binary compounds consisting of InAs, GaSb, and AlSb, among which the differences in lattice parameter are relatively small. (The 6.1 Å refers to their approximate lattice parameter.) Materials also include ternary and quaternary compounds of these elements formed by alloying InSb, GaAs, or AlAs within the 6.1-Å family. The *n*B*n* layer structure is strain balanced to match the GaSb substrate. The absorber is the most critical region of the device because it is the place of origin of photocurrent and most of the dark current, and its bandgap determines the wavelength sensitivity. The primary motivation for using

(Received January 9, 2016; accepted April 13, 2016; published online April 28, 2016)

a superlattice to build the absorber is to decouple the bandgap from the lattice parameter. In contrast, for a bulk ternary alloy, the choice of the lattice parameter constrains the bandgap. By adjusting the thickness and composition of the superlattice layers, one can form a strain-balanced semiconductor material having almost any desired bandgap while maintaining lattice match to the substrate. In the devices we address here, the absorber consists of alternating layers of InAs and InAsSb.

To advance this technology, it has been necessary to acquire better understanding of the origins of the dark current and the characteristics of the materials composing nBn devices. In this paper, we show that measurements of device capacitance as a function of bias and temperature, when combined with direct-current (dc) measurements of the dark current, can be very revealing. To begin, we determine the doping density of the absorber and the depletion width as a function of bias. Then, by plotting dark current density versus depletion width, we are able to separate clearly the two principal components of the dark current, namely current from the depletion region, and current from the neutral region of the absorber. Next, we extract the activation energies of these components and compare them with the activation energies of the conventionally measured dark current, to show that the dark current in this sample is always a mixture of the two current components. Furthermore, from each dark current component, we make an estimate of the minority-carrier lifetime. In addition, we measure the doping density of the barrier material itself.

EXPERIMENTAL PROCEDURES

Device Structure

Figure 1 shows a qualitative sketch of the band profile of the nBn device. E_c, E_F, and E_v are the conduction-band edge, the Fermi level, and the valence-band edge, respectively. A negative bias V is applied to the contact, as in normal operation, causing the offset of the Fermi level between the two ends of the device. The buffer layer and substrate are on the left but not shown. Our measurements (below) establish that the barrier is p-type with much greater concentration than the n-type doping of the absorber. Consequently, the depletion region (width x_1) that occurs due to the p–n junction at the barrier–absorber interface is almost entirely confined to the absorber. Its width increases as the bias is driven more negative. Two origins of dark current are illustrated. The Shockley–Read–Hall (SRH) mechanism creates electron–hole pairs in the depletion region through midgap trap sites, producing a current J_{GR} (generation–recombination). The diffusion current J_{diff} consists of holes diffusing from the neutral region of the absorber toward the depletion region.

The nBn concept was assumed, in early work, to confine the depletion region (or regions) to the wide-

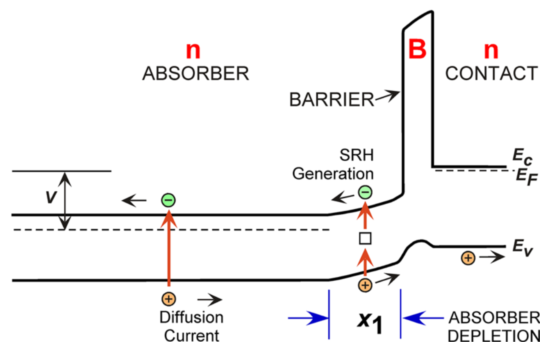

Fig. 1. Sketch of band profile of nBn detector. Two dark current mechanisms are illustrated. A negative bias V applied to the contact causes the offset of the Fermi level and attracts holes to the contact. There are two depletion regions, the first residing within the absorber as shown, and the other consisting of the thin barrier itself. Both depletion regions act as capacitors in response to an oscillatory voltage. The buffer layer and substrate are to the left but not shown.

bandgap barrier. The original paper by Maimon et al.[9] states that "the nBn device operates with the n-type layers in flatband or with only very little depletion," and "The nBn structure essentially eliminates the SRH current." However, this is true only if the doping in the barrier is low compared with the doping in the absorber and contact. In the device addressed below, we find a more complex situation, in which the p-type barrier doping concentration is intermediate between that of a highly doped n-type contact on one side and that of a very low-doped n-type absorber on the other side. In equilibrium, the thin barrier will be fully depleted due to the adjacent contact, but when negative bias is applied to the contact for normal operation, a depletion region will expand into the absorber.

Device Composition and Fabrication

The layer structures were designed and grown by molecular-beam epitaxy (MBE) at Sandia National Laboratories, and the devices were fabricated and tested at Raytheon Vision Systems. Most of the results reported here are from wafer EB3884, having the following layers: First, on the n-type GaSb substrate, there is a GaSb buffer layer. Second is the superlattice absorber composed of 1200 periods of 4.9-nm InAs and 1.8-nm $InAs_{0.67}Sb_{0.33}$ for total thickness of 8.0 μm, with no intentional doping. The structure is strain balanced and lattice matched to the substrate. Next is the barrier of AlGaAsSb with thickness of 0.1 μm. This is mostly AlSb with small amounts of Ga and As added to adjust the valence-band alignment while maintaining lattice matching. The barrier is unintentionally doped but turns out to be p-type. Finally, there is the cap (contact) composed of lattice-matched InAsSb alloy having thickness of 0.15 μm and n-type Si doping of 1×10^{18} cm^{-3}. The sensing elements were delineated by mesa etching, to a depth extending past the barrier. Surfaces were

passivated with plasma-deposited silicon dioxide. Test structures were formed on the wafers at the same time as detector arrays. After dicing, each selected test structure was hybridized by means of indium bumps to a fanout board having metal traces connected to bonding pads, forming a test structure assembly (TSA). The TSA was then wire-bonded in a leadless chip carrier (LCC) for testing with the back side (substrate) facing out from the LCC. In tests requiring illumination, the photons enter through the substrate, which was not removed or thinned. We refer to each sensing element as a diode because it is a two-terminal device. The TSA contains some miniarrays, and a set of 12 variable-area diodes, of square shape, having widths ranging from 25 μm to 800 μm. The data reported here are mostly from TSA number 692521, which was selected for detailed capacitance testing.

Another sample, wafer EB4649, was prepared especially for measurement of barrier doping. After the GaSb substrate and GaSb buffer, a lattice-matched highly conducting InAsSb layer with thickness of 1.0 μm was grown for ohmic access. It was doped p-type with Be at 1×10^{18} cm^{-3}. Next the barrier material was grown 1.0 μm thick, with the same composition as the conventional 0.1-μm barrier in nBn devices. This was followed by a thin (0.015 μm) protective cap of GaSb. Then, metal–insulator–semiconductor (MIS) devices were fabricated with 0.25 μm of plasma-deposited silicon dioxide, followed by metal pads and indium bumps. Parts were subjected to the above-described dicing, hybridization, and wire bonding. The purpose of the ohmic access layer was to minimize series resistance when measuring the capacitance of the MIS devices.

Measurements

The spectral response per photon of wafer EB3884 was measured by conventional Fourier-transform infrared (FTIR) methods. Figure 2 shows an example at temperature $T = 120$ K as a function of photon energy, along with its second derivative. The latter crosses zero at the inflection point, which is a good approximation to the bandgap energy. We find $E_g = 213$ meV.

Capacitance measurements on the nBn devices were made in zero field of view at 150 K, 135 K, 120 K, 105 K, and 90 K, as a function of dc bias. In response to a small oscillatory voltage, the depletion regions act as capacitors. In our case, the net capacitance will be the series combination of the absorber depletion (Fig. 1) and that of the depleted barrier. The test equipment models the device as an ideal capacitance C in parallel with an ideal conductance G. The admittance of the device is then

$$Y = G + iB, \quad (1)$$

where the capacitive susceptance is $B = 2\pi fC$ and f is the frequency, with $i = \sqrt{-1}$. Accurate

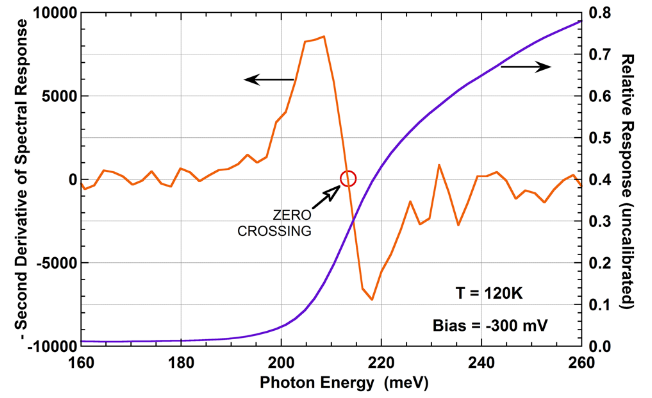

Fig. 2. Spectral response, and its second derivative, versus photon energy for wafer EB3884 at temperature of 120 K. The zero crossing of the second derivative locates the inflection point, which is a very good approximation to the bandgap energy, at a value of 213 meV.

capacitance is obtained only if the capacitance term is much larger than the conductance term. Equivalently, we prefer the phase angle of the admittance, arctan(B/G), to be greater than 80°. A frequency of 10 kHz was found to be suitable for the nBn measurements, because this gives a sufficiently large capacitance term, while a frequency of 1 MHz turned out to be too high because the parasitic effects became unmanageable.

Figure 3 shows a plot of the capacitance versus bias at several temperatures. (This is the combined capacitance of the barrier and absorber, but corrected for the parasitic capacitance as explained below.) The nBn mesa is a square 800 μm wide (area $A = 6.4 \times 10^{-3}$ cm^2). The modulation amplitude is 10 mV. Capacitance falls as bias becomes more negative due to the widening depletion region within the absorber. In positive bias, however, the capacitance remains high because the high doping of the contact precludes any perceptible depletion at the barrier–contact interface. Figure 3 also shows the conductance at the same temperatures. The plots at 105 K and 90 K are noisy because the conductance term is small. The phase angle of the admittance remains well above 85° for nearly all conditions of bias and temperature. Figure 4 shows A/G measured at 10 kHz frequency compared with the conventional dc resistance–area (RA) product $(\mathrm{d}J/\mathrm{d}V)^{-1}$. We find excellent agreement, without having to make any scale adjustments, throughout the full range of bias. This agreement helps to confirm the validity of the oscillatory measurement.

The traces on the fanout of the TSA and the leads in the dewar will add a parasitic capacitance to the measurement. At 10 kHz, this can be corrected with the approximation that

$$C_{\mathrm{tot}} = C + C_{\mathrm{par}}, \quad (2)$$

where C_{tot} is the total measured capacitance, C is the true capacitance of the device, and C_{par} is the parasitic term. The correction was determined using

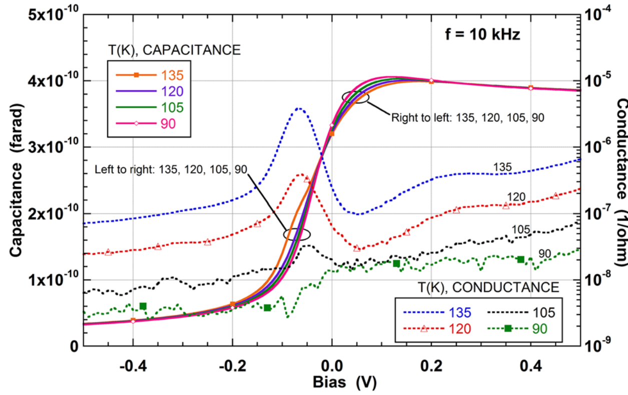

Fig. 3. Capacitance (solid) and conductance (dotted) versus bias at several temperatures. Capacitance declines as bias goes more negative due to the increasing width of the depletion region in the absorber. The correction for parasitic capacitance has been applied. Wafer EB3884.

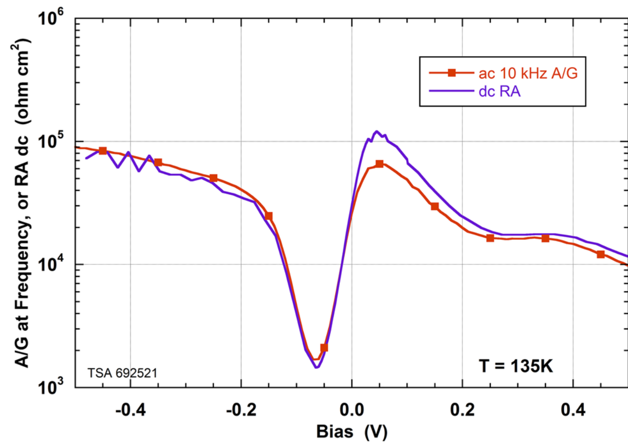

Fig. 4. Reciprocal conductance multiplied by area, measured at 10 kHz, compared with the dc RA product. The two independent measurements agree very well with no scale adjustments. Wafer EB3884.

a set of variable-area diodes. At given bias, we take the experimentally measured capacitance, divide by the respective diode area, and plot the values against 1/A. The relation that will be fit to the plot is obtained by dividing Eq. 2 by diode area.

$$\frac{C_{\rm tot}}{A} = \frac{C}{A} + C_{\rm par}\left(\frac{1}{A}\right). \tag{3}$$

The slope gives the parasitic capacitance, and the intercept is the true capacitance per unit area (at the particular bias). This was done for four different biases, and the slopes were averaged to give $C_{\rm par} = 1.075 \times 10^{-11}$ F. The parasitic component overwhelms the signal from the smallest diodes, but on the 800-μm diode (referring to Fig. 3), the correction was only about 13% at -0.2 V and only 3% at +0.2 V near the maximum. The parasitic

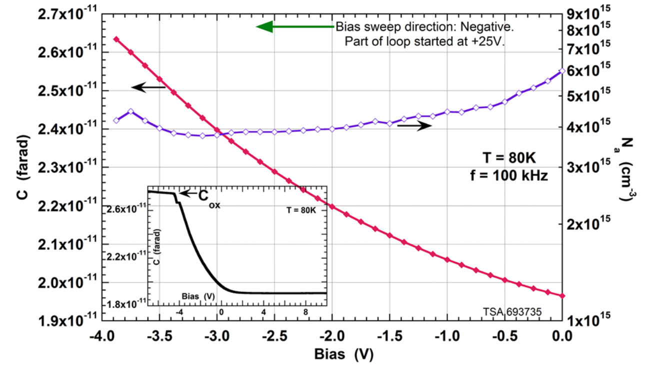

Fig. 5. Capacitance measurement on the special MIS sample, wafer EB4649. The left axis indicates the capacitance in the transition from depletion to accumulation (in a negative-going bias sweep). From this, the acceptor concentration in the barrier material (right axis) is found to be about 4×10^{15} cm^{-3}. The C–V curve in the inset sweeps through a wider range, reaching full oxide capacitance at negative bias, confirming that the barrier material is p-type.

capacitance was subtracted before proceeding with the analysis.

The next step was to account for the capacitance of the depleted barrier.[10] Assuming the relative dielectric constant to be 12.04 (the same as for AlSb), with thickness of 0.1 μm, the barrier capacitance on the 800-μm diode becomes 6.84×10^{-10} F. Then, using the conventional sum-of-reciprocals relationship for capacitors in series, the capacitance of the absorber depletion region alone was determined. The analysis in the following section is based upon the absorber depletion capacitance.

Doping of the barrier was measured with the MIS devices on the special wafer described above (EB4649). Figure 5 shows part of a C–V trace and the resulting acceptor concentration calculated according to conventional methods.[11] The metal contact area in this case was a square 460 μm wide, and the relative dielectric constant was taken, as above, to be 12.04. From a set of varying-area metal pads, the parasitic capacitance was determined according to Eq. 3 to be 4.89×10^{-12} F. The doping level (Fig. 5) was found to be approximately 4×10^{15} cm^{-3}. We conclude that it is p-type, because the full oxide capacitance, due to accumulation at the AlGaAsSb–SiO_2 interface, is reached as bias goes more negative (inset of Fig. 5). The 1.0 μm thickness of the barrier material was sufficient for this experiment because the maximum depletion implied by the C–V plot[11] is 0.63 μm.

RESULTS AND DISCUSSION

Dark Current and Capacitance Analysis

Figure 6 shows the dark current density of the nBn device in negative bias for a variety of temperatures. (The following results are for the above-described wafer EB3884.) When bias is more negative than about -0.2 V, the J–V curves at the higher temperatures exhibit a very small slope, indicating

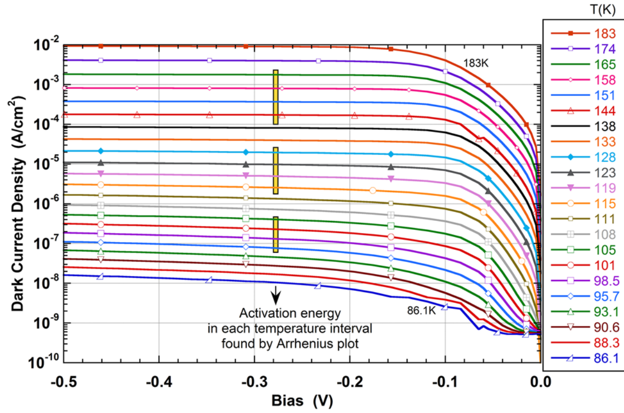

Fig. 6. Dark current density versus bias at multiple temperatures. The narrow rectangles are examples of small regions of the temperature–bias parameter space in which an activation energy will be calculated. A bias more negative than −0.12 V is required for full turn-on. Curves appear in the same order from top to bottom as their corresponding temperatures in the legend. Wafer EB3884.

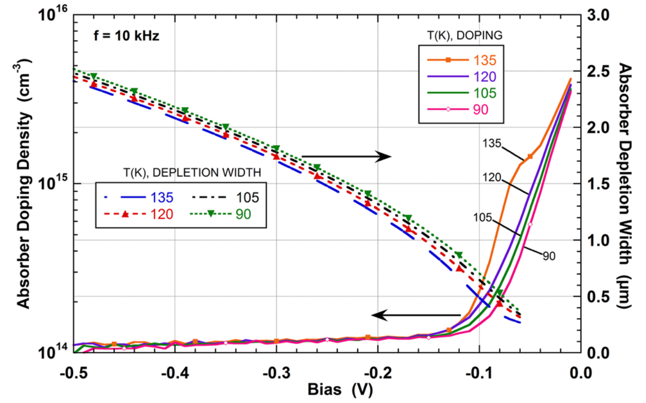

Fig. 7. Donor density in the absorber (solid) and width of the depletion region in the absorber (dashed), both derived from the *C*–*V* measurements. Reliable values occur beyond the −0.12 V turn-on, with an average doping of 1.2 × 10^{14} cm^{-3}. Wafer EB3884.

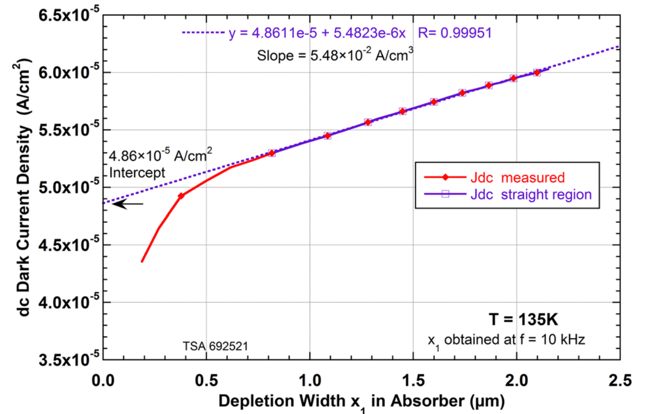

Fig. 8. Dark current density measured at dc, versus the depletion width in the absorber measured at 10 kHz, at 135 K. The remarkable feature is the existence of a straight region, which represents the GR component of the dark current. Wafer EB3884.

diffusion-dominated current but with a small GR contribution. At the lower temperatures, the relative slopes are greater, suggesting a larger proportion of GR current. A quantitative measure of the mix between diffusion and GR will be inferred by means of the capacitance results obtained below. When bias is between 0 V and −0.12 V, the device is not fully turned on and the behavior is more complicated. At zero bias we estimate that the valence-band edge is at least 100 meV lower in the contact than in the absorber, due to the differences in bandgap and doping. This offset must be overcome by the applied bias (sketched in Fig. 1) to achieve turn-on.

To analyze the *C*–*V* characteristics of the absorber depletion region, we assume that a one-sided abrupt junction exists between the barrier and absorber, and apply the following textbook equation[12]:

$$\frac{C}{A} = \frac{\varepsilon_s}{x_1} = \sqrt{\frac{q\varepsilon_s N_{d1}}{2(V_{bi} - V)}}, \quad (4)$$

where ε_s is the semiconductor dielectric constant (assumed to be $15.15\varepsilon_0$, the same as for InAs), ε_0 is the vacuum permittivity, x_1 is the thickness of the depletion region, N_{d1} is the donor doping, V_{bi} is the built-in voltage, and q is the unit charge. This leads to an expression for the doping[10,13]:

$$N_{d1} = \frac{2}{q\varepsilon_s A^2 \frac{d(1/C^2)}{dV}}. \quad (5)$$

The result appears in Fig. 7. Beyond the turn-on bias, we find the doping to be uniform and independent of temperature (as expected) with an average of 1.2 × 10^{14} cm^{-3}. This is lower than the barrier doping by a factor of 33, making the assumption of a one-sided abrupt junction reasonable but not ideal. Although a ratio greater than 100 would be preferred, the consequent error in doping should be well below 10%. Additionally, the depletion width can be found from the capacitance by Eq. 4, giving the result displayed also in Fig. 7. The surprisingly wide depletion of 2.5 μm at −0.5 V is a consequence of the low doping.

It is instructive to combine the 10 kHz measurement of depletion width and the dc measurement of dark current density. The result at 135 K is displayed in Fig. 8. The remarkable feature is that, from the data of the two independent curving plots (Figs. 6 and 7), we find a very straight region in Fig. 8. Current is rising linearly as the absorber depletion region becomes wider. The slope implies a generation rate of 5.48 × 10^{-2} A/cm^3. Because this is a linear function of depletion width, we interpret it to be the GR current, due to generation via midgap states according to the SRH mechanism. Furthermore, we can extrapolate this straight line to the left axis to represent the hypothetical case of

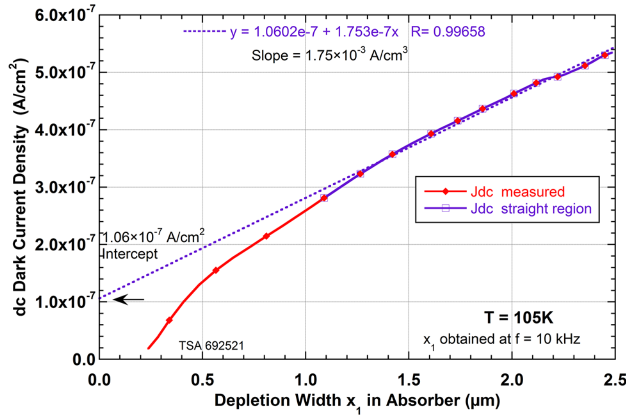

Fig. 9. Dark current density measured at dc, versus the depletion width in the absorber measured at 10 kHz, at 105 K. The features observed in the previous figure are repeated at other temperatures. Wafer EB3884.

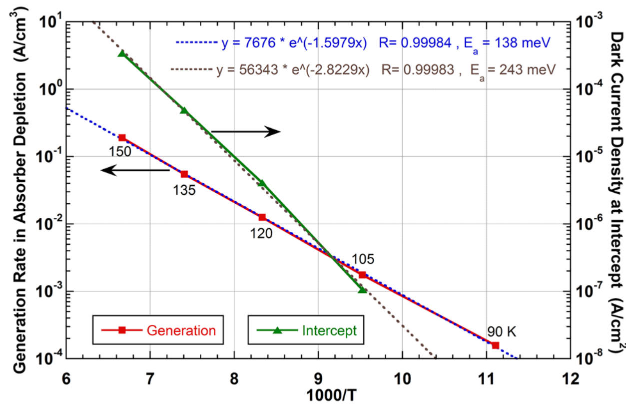

Fig. 10. Arrhenius plots for the two basic dark current components. Resulting activation energies are 138 meV for GR and 243 meV for diffusion. Wafer EB3884.

zero depletion of the absorber. The intercept, in our interpretation, is a good approximation to the diffusion current density, in this case 4.86×10^{-5} A/cm^2. (The interval between 0 μm and 1.0 μm is modified by the turn-on conditions.) The same kind of behavior occurs at other temperatures; For example, Fig. 9 shows the result at 105 K, indicating a rate of 1.75×10^{-3} A/cm^3 for GR and a diffusion current density of 1.06×10^{-7} A/cm^2.

Figure 10 shows an Arrhenius plot of the generation rate (left axis) versus temperature. On the interval $90\,\text{K} \leq T \leq 150\,\text{K}$, there is an excellent fit to the exponential, yielding an activation energy of 138 meV, which is close to half the bandgap. The right axis in Fig. 10 refers to the Arrhenius plot for the presumed diffusion current ($105\,\text{K} \leq T \leq 150\,\text{K}$), giving an activation energy of 243 meV, which is near the bandgap energy. To give a perspective on the dark currents, the diffusion current in Fig. 10 exceeds the HgCdTe Rule 07 value[14] by a factor of 5 at 150 K. When the GR mechanism is included, the total dark current is certainly higher than optimum, and would benefit from minimization of the absorber depletion. The dominance of GR becomes evident at the lower temperatures, and at 90 K the diffusion component cannot be resolved beneath the GR current.

Temperature prefactors must be taken into account for a more accurate assessment of the activation energies. The temperature dependences of the diffusion and GR currents, respectively, are given by[15,16]

$$J_{\text{diff}} \sim T^3 \exp\frac{-E_g}{kT},$$

$$J_{\text{GR}} \sim T^{3/2} \exp\frac{-E_g}{2kT}, \tag{6}$$

where k is Boltzmann's constant. This can be generalized to

$$J_m \sim T^{3/m} \exp\frac{-E_g}{mkT} \approx H \exp\frac{-E_a}{kT}, \tag{7}$$

where $m = 1$ for diffusion, $m = 2$ for GR, and E_a is an activation energy. For a given temperature interval, we make the assumption that on the right-hand side all of the temperature dependence can be incorporated into the exponential factor, so that H will be independent of temperature. This is a reasonable approximation because the plots of Fig. 10 show very little curvature, and thus no need for a temperature prefactor to obtain a good fit. We take the logarithm of Eq. 7 and differentiate with respect to $1/T$. The result is

$$E_a \approx \frac{3}{m}kT + \frac{E_g}{m}. \tag{8}$$

The right-hand side of this equation is to be compared with the experimentally obtained activation energies from Fig. 10. We take $T = 120$ K, representing the middle of the temperature interval, and 213 meV for the bandgap of the absorber according to Fig. 2. Then, in the case of diffusion ($m = 1$), Eq. 8 gives 244 meV, in good agreement with the 243 meV for the diffusion current activation from Fig. 10. In the case of GR ($m = 2$), Eq. 8 gives 122 meV, in approximate agreement with the 138 meV found from the GR activation in Fig. 10.

In summary, a significant result has been reached. The GR dark current component originating in the depletion region of the absorber has been unambiguously identified, because (a) it is a linear function of the depletion width, and (b) its activation energy is approximately half the bandgap. The remaining dark current, moreover, can be identified with the diffusion current from the neutral part of the absorber because its activation energy matches the bandgap. Surface currents were shown to be negligible in this sample because the total dark current density was independent of area for the large diodes of the variable-area set.

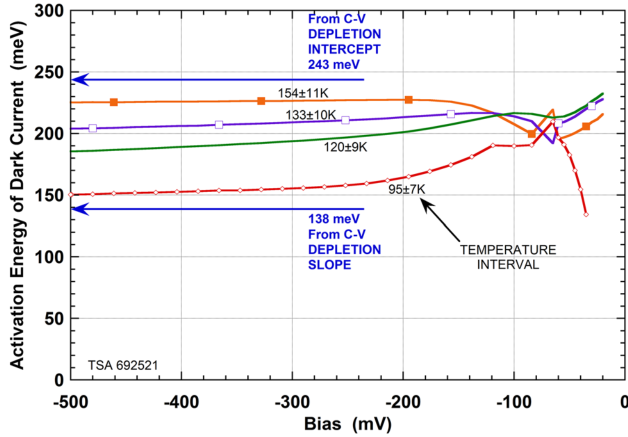

Fig. 11. Activation energies of the total measured dark current, for selected temperature intervals, as functions of bias. Upper and lower bounds for these curves are defined by the activation energies of the two basic components of the dark current, which have been determined through the *C–V* measurements. Wafer EB3884.

Activation Energy of Dark Current and Lifetime of Minority Carriers

The activation energies that we have found for the two separate components of dark current can serve as reference points for assessment of the total measured dark current. Referring to Fig. 6, the narrow rectangles conceptually define temperature intervals over which a local activation energy of the dark current density can be calculated. (The term "local" denotes a limited region of the temperature–bias parameter space.) This calculation is repeated at each available bias value. The results are presented in Fig. 11. Each curve is labeled by the middle temperature of its interval. The higher temperatures show a larger activation energy indicative of diffusion dominance, while the lower temperatures indicate GR dominance. (All of the curves in Fig. 11 were calculated without dividing by a temperature prefactor, which cannot be specified uniquely.) The two horizontal arrows point to the activation energies of the basic current components, determined as explained above. They form upper and lower bounds for all of the activation energies of the total current density. The conclusion is that, at any temperature and bias, the dark current is a mixture of the two basic components with the proportions indicated by the local activation energy.

Having values for the two basic dark current components will enable rough estimates of the minority-carrier lifetimes. The GR depletion current originating in a reverse-biased junction is reasonably approximated by

$$J_{\mathrm{GR}} = \frac{qn_{\mathrm{i}}x_1}{2\tau}, \tag{9}$$

where n_{i} is the intrinsic carrier concentration and $\tau = \sqrt{\tau_{n0}\tau_{p0}}$ is the combined carrier lifetime. Equation 9 is derived by simplifying the full equation for GR current[17] with the assumptions that the active traps are near midgap, and that the magnitude of the reverse bias is large compared with both the built-in voltage and kT/q. The factor of 2 in the denominator originates when dropping the smaller of two exponentials in the hyperbolic sine function of the full GR equation. The straight slopes in Figs. 8 and 9 are equivalent to $\mathrm{d}J_{\mathrm{GR}}/\mathrm{d}x_1 = qn_{\mathrm{i}}/(2\tau)$. This is the generation rate, according to which an incremental increase of the depletion width in the absorber produces an increment of GR current density. We consider the result at 150 K, where the generation rate is 0.190 A/cm^3. We estimate that $n_{\mathrm{i}} = 4.2 \times 10^{13}$ cm^{-3} (at 150 K) according to the standard formula,[12] by assuming the relative effective masses $m_{\mathrm{e}}^* = 0.028$ and $m_{\mathrm{h}}^* = 0.300$, for electrons and holes, respectively (Ting, private communication, 2014). These are the density-of-states effective masses, which are not the same as the mobility effective masses. The result is $\tau = 18$ μs. This is comparable to other very good lifetimes in MWIR InAs/InAsSb superlattice samples, which have been measured by the preferred time-resolved techniques of differential transmission or photoluminescence.[18,19]

A minority-carrier lifetime can also be inferred from the diffusion saturation current according to[15,16]

$$\tau = \frac{qn_{\mathrm{i}}^2 d}{N_{\mathrm{d1}}J_{\mathrm{diff}}}, \tag{10}$$

where d is the thickness of the neutral region in which the current originates. Again we consider the case of $T = 150$ K, where we have obtained $J_{\mathrm{diff}} = 3.41 \times 10^{-4}$ A/cm^2. We take $d = 6$ μm, based on the absorber thickness (8 μm) minus the strong-bias depletion thickness (about 2 μm). The donor concentration is $N_{\mathrm{d1}} = 1.2 \times 10^{14}$ cm^{-3} (Fig. 7). The result is $\tau = 4$ μs. Since different mechanisms are involved, the two lifetime estimates do not have to be equal, but they are both approximately on the order of 10 μs.

CONCLUSIONS

We have demonstrated a method for clearly separating out the GR component of the dark current, which originates by the SRH mechanism in the depletion region of the *n*B*n* device. This is done by plotting the conventional dc measurement of dark current density against the depletion width revealed by capacitance testing. The identity of the GR component is validated by two characteristics: its linear dependence on depletion width, and its thermal activation energy approximately equaling one-half the bandgap. The remaining current, which was defined by extrapolating to zero depletion width, is shown to be the diffusion current component that originates in the neutral region of

the absorber. Its identity is confirmed by an activation energy nearly equal to the full bandgap. Also, we have shown that the activation energies of these two current components form upper and lower bounds for the local activation energies of the total measured dark current density. This means that, at any bias (beyond the turn-on region) and any temperature, the actual dark current is a superposition of the two components, with relative proportions that can be approximately estimated according to how the local activation energy is positioned between these bounds.

Furthermore, we have found that the MWIR wafer EB3884 is of very high quality. Having no intentional doping, the InAs/InAsSb absorber is *n*-type with carrier concentration of only 1.2×10^{14} cm^{-3}, indicative of a very clean MBE process. Its minority-carrier lifetime is found to be on the order of 10 μs, which is similar to some of the best reported values for this kind of material.[18,19] In addition, we have measured the carrier concentration of the unintentionally doped barrier material of the *n*B*n*, finding it to be *p*-type at 4×10^{15} cm^{-3}.

ACKNOWLEDGEMENTS

This work was supported by the Air Force Research Laboratory, Space Vehicles Directorate. The Contracting Officer's Technical Representative is Dr. Christian Morath. Sandia National Laboratories is a multiprogram laboratory managed and operated by Sandia Corporation, a wholly owned subsidiary of Lockheed Martin Corporation, for the US Department of Energy's National Nuclear Security Administration under Contract DE-AC04-94AL85000.

CONFLICT OF INTEREST

The authors declare that they have no conflict of interest.

REFERENCES

1. A. Haddadi, R. Chevallier, G. Chen, A.M. Hoang, and M. Razeghi, *Appl. Phys. Lett.* 106, 011104 (2015).
2. C.P. Morath, V.M. Cowan, L.A. Treider, G.D. Jenkins, and J.E. Hubbs, *IEEE Trans., Nucl. Sci.* 62, 512 (2015).
3. Y. Aytac, B.V. Olson, J.K. Kim, E.A. Shaner, S.D. Hawkins, J.F. Klem, M.E. Flatte, and T.F. Boggess, *J. Appl. Phys.* 118, 125701 (2015).
4. P.C. Klipstein, E. Avnon, Y. Benny, A. Fraenkel, A. Glozman, E. Hojman, E. Ilan, E. Kahanov, O. Klin, L. Langof, Y. Livneh, I. Lukomsky, M. Nitzani, L. Shkedy, I. Shtrichman, N. Snapi, R. Talmor, A. Tuito, S. Vaserman, and E. Weiss, *Proc. SPIE* 9451, 94510K (2015).
5. M.A. Kinch, *J. Electron. Mater.* 44, 2969 (2015).
6. P.T. Webster, N.A. Riordan, S. Liu, E.H. Steenbergen, R.A. Synowicki, Y.-H. Zhang, and S.R. Johnson, *Appl. Phys. Lett.* 106, 061907 (2015).
7. D.Z. Ting, A. Soibel, S.B. Rafol, J. Nguyen, L. Hoglund, A. Khoshakhlagh, S.A. Keo, J.K. Liu, J.M. Mumolo, and S.D. Gunapala, *Proc. SPIE* 8012, 801214 (2011).
8. D.Z. Ting, A. Soibel, L. Hoglund, and S.D. Gunapala, *J. Electron. Mater.* 44, 3036 (2015).
9. S. Maimon and G.W. Wicks, *Appl. Phys. Lett.* 89, 151109 (2006).
10. J.F. Klem, J.K. Kim, M.J. Cich, S.D. Hawkins, T.R. Fortune, and J.L. Rienstra, *Proc. SPIE* 7608, 76081P (2010).
11. E.H. Nicollian and J.R. Brews, *MOS (Metal Oxide Semiconductor) Physics and Technology* (New York: Wiley, 1982), p. 385.
12. B.G. Streetman, *Solid State Electronic Devices*, 2nd ed. (Englewood Cliffs, NJ: Prentice-Hall, 1980), p. 75, 175.
13. A.S. Grove, *Physics and Technology of Semiconductor Devices* (New York: Wiley, 1967), p. 171.
14. W.E. Tennant, D. Lee, M. Zandian, E. Piquette, and M. Carmody, *J. Electron. Mater.* 37, 1406 (2008).
15. S.M. Sze, *Physics of Semiconductor Devices*, 1st ed. (New York: Wiley, 1969), p. 102.
16. S.M. Sze and K.K. Ng, *Physics of Semiconductor Devices*, 3rd ed. (New York: Wiley, 2007), p. 95.
17. C.-T. Sah, R.N. Noyce, and W. Shockley, *Proc. IRE* 45, 1228 (1957).
18. B.V. Olson, E.A. Shaner, J.K. Kim, J.F. Klem, S.D. Hawkins, L.M. Murray, J.P. Prineas, M.E. Flatte, and T.F. Boggess, *Appl. Phys. Lett.* 101, 092109 (2012).
19. B.C. Connelly, G.D. Metcalfe, H. Shen, and M. Wraback, *Proc. SPIE* 8704, 87040V (2013).